VI International Conference on Computational Methods in Marine Engineering
MARINE 2015
F. Salvatore, R. Broglia and R. Muscari (Eds)

# Investigation of Tunnel Thruster Performance and Flow by Quasi-Steady and Unsteady RANS Simulations

**Cheng Yu*, Chen-Jun Yang***

*State Key Laboratory of Ocean Engineering,
Shanghai Jiao Tong University, Shanghai 200240, China
e-mail:cjyang@sjtu.edu.cn

**Key words:** tunnel thruster, RANS, quasi-steady, unsteady, numerical blockage effect

**Abstract.** Two numerical models based on the solution of the RANS equations using the SST $k$-$\omega$ turbulence model have been employed to investigate the hydrodynamic performance and flow of tunnel thrusters. The flow passages between adjacent blades are discretized with prismatic cells so that the boundary layer flow is resolved down to the viscous sub-layer. For three impellers covering a range of extended area ratio and pitch ratio the hydrodynamic performances predicted by the quasi-steady model agree well with experimental data. Unsteady simulations are also performed by using the sliding mesh model, and the results are compared with those of the quasi-steady model to investigate the influences of the quasi-steady approximation on predicted loads. Through analysis of the flow field, the reason why the hub of impeller contributes a small amount of thrust, and how the impeller induces an axial force on the hull, which can amount to 40~60% of the impeller thrust, are made clear. Besides, several flow features of interest are investigated based on the simulation results.

## 1 INTRODUCTION

The tunnel thruster consists of an impeller mounted inside a tunnel, which generates in transverse direction the thrust required for manoeuvering and dynamic positioning of the vessel. It is located athwart the vessel in the bow and sometimes at the stern. Due to the high loading on the impeller blades and the interaction of the impeller with the drive unit fairings, the tunnel wall, and the hull, the flow across the tunnel becomes quite complicated and many factors would impact upon the hydrodynamic performance of the tunnel thruster, such as the geometry and location of impeller blades, the length and inlet/exit geometry of the tunnel, the shape of drive unit fairings, protective grids, and flow speed, etc. Usually, the thruster has a controllable pitch, constant speed impeller or a fixed pitch, variable speed one. Both of them often have blade sections symmetrical about the nose-tail lines, although in the former case the blade mean surfaces are usually defined on flat surfaces (rather than the usual helical surfaces) and such blades are thus termed 'flat plate blades'[1].

The study of tunnel thruster performance is mostly based on model experiments and empirical data and/or formulas. Pehrsson and Mende[2] proposed a design criterion and an empirical guide to the selection of tunnel thrusters. Taniguchi et al.[3] conducted a systematic experimental study of the effect of various blade geometrical parameters and the influence of

tunnel layout. English[4] pointed out that the transverse force generated by tunnel thrusters under ideal circumstance consists of two parts which are equal in magnitude, i.e. the impeller force and the impeller-induced force on the vessel. However, in practical flow situation, Beveridge[5] found that the impeller force accounts for 52%~87% of the total transverse force. Based on the statistical information of some ships, Ridley[6] found that the efficiency of tunnel thrusters decreases rapidly when a ship advances at low speed. The anti-suction tunnel, which is a smaller tunnel behind the tunnel thrusters, is a good solution to this problem because it can balance the pressure on the port and starboard[7].

When compared with an open propeller, the flow field around the tunnel thruster is more complex and thus more difficult to simulate numerically due to flow separation near the tunnel inlet, the bollard pull condition, and the interactions among different parts of the thruster. On the other hand, there are few public sources of fundamental experimental data for the validation of computational methods. Mainly due to these reasons the numerical study of tunnel thruster performance is insufficient.

Muller and Abdel-Maksoud[8] studied the effect of tunnel length, tunnel entrance, impeller location and the shape of protective grids by the software CFX. Based on the detailed information and analysis of the flow field, some helpful conclusions are drawn such as the most effective tunnel length, the relationship between tunnel inlet configuration and the total thrust and the best protective grid position. For a 'flat plate' Kaplan type controllable-pitch propeller working in an axial cylinder, Stefano, et al.[9] predicted the sheet cavitation on propeller blades using a boundary element method and conducted experimental observations of the cavity geometry as well as measurements of the hydrodynamic performance in a cavitation tunnel. Compared with the experiments, the numerical method showed acceptable accuracy except close to the bollard condition due to some intrinsic deficiencies in the potential flow model, as pointed out by the authors. Using the software FLUENT, Yao and Yan[10] studied the influence of some geometric parameters on tunnel thruster performance, as well as the performance under different ship speeds which is in accordance with the conclusions drawn by Ridley[6].

Design of the tunnel thruster is a challenging task in view of several aspects which affect the thruster's performances. Due to thruster-hull interaction the hull contributes to the axial force, which needs to be considered for accurate design of the tunnel thruster. The heavily loaded thruster blades interact strongly with the blunt gear housing and the tunnel wall, which may induce cavitation, pressure fluctuation, and structure vibration. These problems are not much investigated to date. On the other hand, the established methods based on the potential flow theory are not adequate enough for tunnel thrusters due to their limited capability to deal with the thruster/hull, blade/gear-housing, and blade/tunnel-wall interactions. Viscous flow CFD methods are better options though they are quite computationally intensive and demanding. Before developing any RANS-based design methodology for the tunnel thruster, it seems necessary to have a RANS tool for more reliable and accurate evaluation of the tunnel thruster performance, and to investigate the flow for a better understanding of the hydrodynamic interactions existing in the tunnel thruster.

In this paper, RANS simulations are carried out for three tunnel thruster models experimentally investigated by Taniguchi, et al.[3]. The Kaplan type impeller blades are of controllable pitch. The effects of blade pitch and area are systematically investigated. Based on the numerically results, the flow is analyzed to understand why and how the hull and the

hub contribute to the axial force. Furthermore, the unsteady forces and fluctuating pressures simulated under non-cavitating condition are investigated.

## 2 THRUSTER GEOMETRY AND SETUP IN TANIGUCHI'S EXPERIMENTS

Taniguchi, et al.[3] published the towing tank test results of a series of tunnel thruster models. Three of the impeller models, No. 1322, 1308, and 1323, of which the extended area ratio, $A_E/A_O$, equals to 0.3, 0.45, and 0.6 respectively, are selected for the present research. The impellers are all four-bladed with a diameter, $D$, of 200mm, and a hub ratio, $dh/D$, of 0.4. As illustrated in Figure 1, the impeller blades are of Kaplan type, and slightly skewed. The chord length and the mid-chord location are both linear with the radius and can be calculated by the following relations,

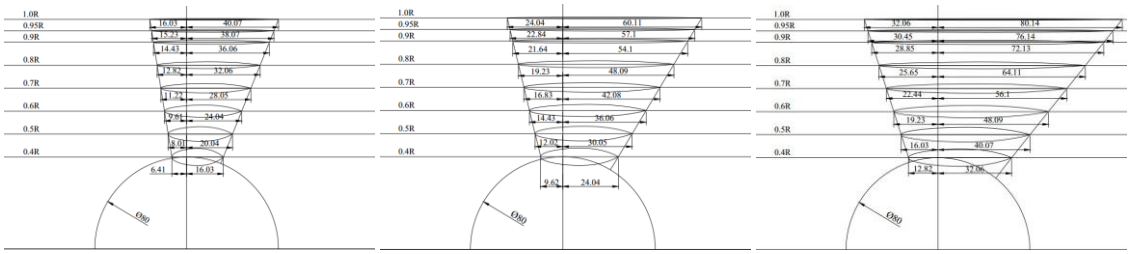

**Figure 1.** The extended outlines of impeller models No. 1322, $A_E/A_O$=0.3 (left), No. 1308, $A_E/A_O$=0.45 (middle), and No. 1323, $A_E/A_O$=0.6 (right).

$$\left.\begin{aligned} \frac{C(\bar{r})}{D} &= \frac{\pi}{3.36}\frac{A_E}{A_O}\bar{r} \\ C_{GL}(\bar{r}) &= C(\bar{r})/3 \end{aligned}\right\} \tag{1}$$

where $\bar{r}=\frac{r}{R}, R=D/2$. $C(\bar{r})$ and $C_{GL}(\bar{r})$ denote the chord length and the chordwise distance from the leading edge to the generator line, respectively. The impeller blades are 'flat plates', i.e. the mean surfaces of the impeller blades are initially defined on a flat surface perpendicular to the impeller shaft axis. The symmetrical blade sections at different radii take the shape of the NACA16 profile. The maximum thickness of a blade section at radius $\bar{r}$ can be calculated by the following relation,

$$\frac{t_{\max}(\bar{r})}{D} = 0.06015 - 0.056625\,\bar{r} \tag{2}$$

The pitch of the impeller blades are controllable, and the pitch ratio at 0.7$R$, $P_{0.7R}/D$, was varied between 0 and 1.3 in the model tests. To set a desired pitch ratio, $(P_{0.7R}/D)_{\text{desired}}$, the blades are rotated about the spindle axis from $P_{0.7R}$=0 by an angle, $\theta$, calculated as

$$\theta = \tan^{-1}\frac{(P_{0.7R}/D)_{\text{desired}}}{0.7\pi} \tag{3}$$

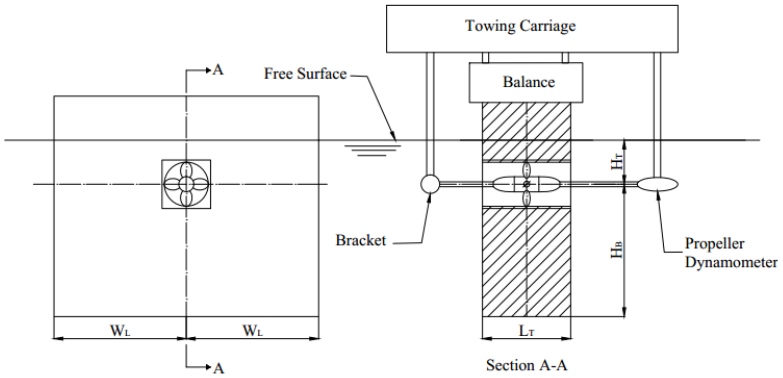


**Figure 2.** The experimental setup for tunnel thrusters, sketched after Taniguchi, *et al.* [3].

Figure 2 illustrates the experimental setup for tunnel thrusters in Taniguchi, et al.[3]. A rectangular block was used as the notional hull. The tunnel was of circular cylindrical geometry, while its entrance (facing the bracket in Section A-A) and exit (facing the propeller dynamometer in Section A-A) were both rounded with a radius of 10mm. As illustrated in Figure 2, the axis of the tunnel (and of the impeller shaft) is located at the center of the hull, and the distances from the axis to port and starboard sides of the hull are both denoted by $W_L$. The distances from the axis to the still water surface and the bottom of the hull are denoted by $H_T$ and $H_B$, respectively. The length of the tunnel is denoted by $L_T$. The length of the hub including its caps and the tip clearance of the impeller blades are denoted by $L_H$ and $W_G$, respectively. The values of these parameters are listed in Table 1.

**Table 1.** Geometric parameters of the notional hull and the tunnel

| | |
|---|---|
| $W_L/D$ | 3 |
| $H_T/D$ | 1.25 |
| $H_B/D$ | 3 |
| $L_T/D$ | 2 |
| $L_H/D$ | 1.5 |
| $W_G$(mm) | 1.5 |

As illustrated in the A-A sectional view of Figure 2, the impeller was supported by brackets at one end and by the shaft of propeller dynamometer at the other. The notional hull was fixed to a balance for measuring the axial force acting on it. The dynamometer, the brackets, and the balance were all fixed to the towing carriage.

The model experiments were conducted at various impeller rotation speeds. Taniguchi, et al.[3] found that the measured axial forces and moment were almost identical for impeller rotation speeds above 600r/min. The experimental results at 900r/min and 1200r/min were presented, and those at 1200r/min are used to compare with the present numerical simulation results. The hydrodynamic performance of tunnel thrusters is presented by using the following non-dimensional coefficients,

$$K_T = \frac{T}{\rho n^2 D^4},\ K_Q = \frac{Q}{\rho n^2 D^5},\ C_F = \frac{F}{\rho n^2 D^4},\ \eta = \frac{[(K_T + C_F)/\pi]^{3/2}}{K_Q} \tag{4}$$

where $T$ is the thrust of the impeller blades and the hub, $Q$ is the torque of the impeller blades, and $F$ is the impeller-induced axial force acting on the hull. $F$ is positive when it is in the same direction as $T$. $\rho$ is water density, $n$ and $D$ are impeller rotation speed and diameter, respectively. The static merit coefficient, $\eta$, is used to evaluate the efficiency of the tunnel thruster unit under the bollard condition.

# 3 NUMERICAL SIMULATION METHOD

## 3.1 Geometric model and grid generation

The geometric model of tunnel thruster is illustrated in the left part of Figure 3 together with the notional hull for the present numerical computations. The hull is defined in a fixed rectangular coordinate system, *O-XYZ*, where the *X* axis coincides with the impeller shaft axis and points toward upstream, the *Y* axis points vertically downwards, and the *Z* axis completes the right-handed system. The origin, *O*, is located at the center of the impeller. The impeller rotates about the *X* axis in its positive direction by the right-hand rule. The geometry, size, and immerged depth of the hull are the same as in the experiments of Taniguchi, *et al.*[3]. To facilitate grid generation, the brackets and the propeller dynamometer have been removed, assuming that their disturbances to the flow are negligible since they were quite far away from the model in the experiments. However, the shafts are retained which extend from the upstream end of the hub cap to 2*D* upstream, and from the downstream one to the outlet of the computational domain, respectively. As illustrated in the right part of Figure 3, the computational domain is a half of a circular cylinder with a diameter of 100*D* and a length of 80*D* in the axial direction. Such large domain sizes are necessary for the RANS simulation under the bollard condition. According to our numerical test results, the present sizes are found large enough to make the influences of inlet and outlet boundary conditions on the solution negligible. The hull is located at the center of the truncated free surface.

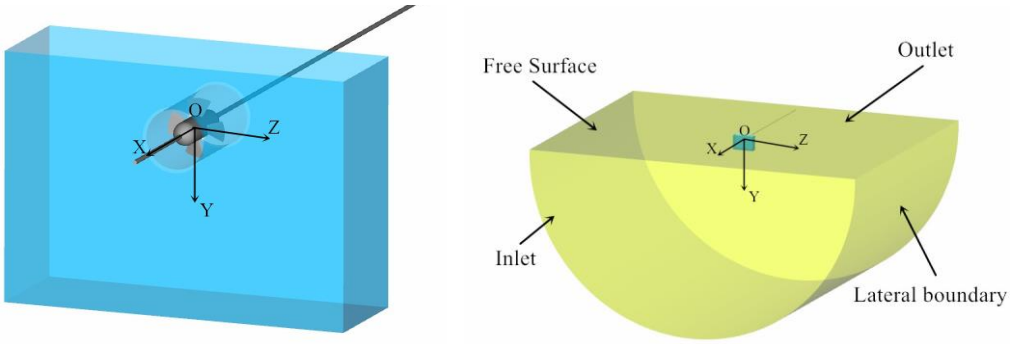


**Figure 3.** The geometric model of tunnel thruster (left) and the computational domain (right).

The computational domain is divided into two parts. The first part contains the impeller blades and the hub, which is defined in a coordinate system O-X'Y'Z' rotating synchronously with the impeller. Initially this rotating coordinate system coincides with the fixed one, O-XYZ. The second part, i.e. the rest of the computational domain, is defined in the fixed coordinate system. In Figure 4 the O-XY section of computational grids inside the tunnel is shown.

To better resolve the boundary layer flow around impeller blade surfaces, an envelope, as shown in Figure 5, is generated around each blade so that prism layer grids are easily generated inside the envelope. The height of the grid layer adjacent to the blade surface is so chosen that $y+\leq 3$. The portions of computational domain between neighboring blades and outside the envelopes are also discretized with prismatic cells along the radial direction, which improves the grid quality.

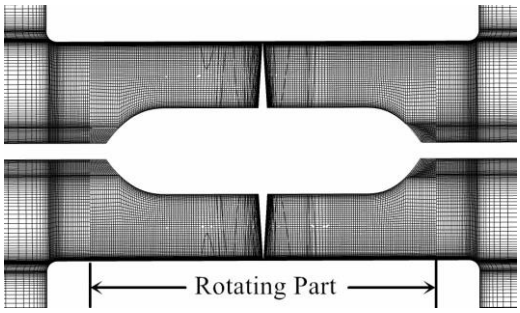


**Figure 4.** Computational grids inside the tunnel.

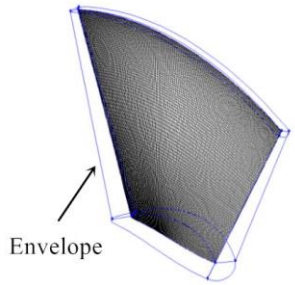


**Figure 5.** The envelope surrounding the blade.

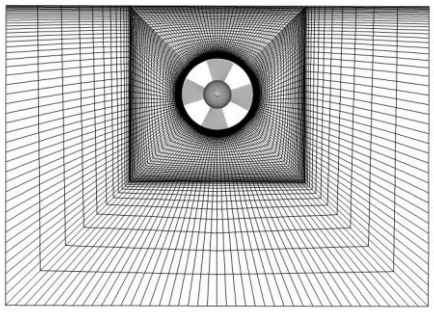

**Figure 6.** Surface grids around the entrance of the tunnel.

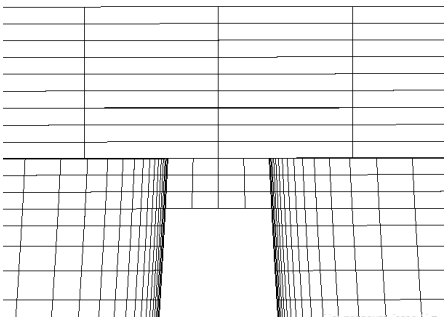

**Figure 7.** Grids around the tip of an impeller blade.

The stationary part of the computational domain is further divided into 110 sub-domains, so that structured grids can be generated in each of the sub-domains. The grids near the entrance and exit of the tunnel are densified to resolve the large gradients of flow quantities, as shown in Figure 6. Due to the complicated flow around impeller blade tips, the computed forces were quite sensitive to the number of grid layers across the tip clearance, i.e. the gap between the tip and the tunnel wall. Numerical tests were conducted and the results indicated that twelve layers were acceptable considering computational stability and accuracy, and were used in all the simulations presented in this paper. An example of the grids in the tip clearance is shown in Figure 7.

The computational grids are generated by using GAMBIT, a pre-processor of the software FLUENT. In total there are about 9 million cells for the entire domain, where 5 million are dedicated to the rotating part.

### 3.2 Computational setup

The flow around tunnel thrusters is simulated by solving the Reynolds Averaged Navier-Stokes (RANS) equations, using the SST k-ω model for turbulence closure. The RANS simulations are conducted by using CFD software FLUENT. For all the governing equations, the second-order upwind scheme is employed to discretize the convection terms. The first-order implicit scheme and non-iterative time advancement technique are used in temporal discretization and time stepping, respectively. The quasi-steady model and the unsteady sliding mesh model are employed to simulate the interactions between the rotating and stationary parts of the computational domain in an approximate and time-accurate manner,

respectively. According to whether the quasi-steady or the unsteady model is selected, the steady or unsteady double-precision pressure-based solver is used. In unsteady simulations the time step size is set as $1.389\times10^{-4}$s, which corresponds to an angular displacement of 1° for the impeller rotating at 1200r/min.

The surfaces of impeller blades, the hub and shafts, the tunnel, and the notional hull are set as stationary walls in their respective coordinate systems. The inlet, outlet, and lateral boundary as designated in Figure 3 are set as velocity inlets. Only bollard condition is simulated in this study, so the inlet velocity is set to zero. Since the impeller works inside the tunnel and the impeller shaft immersion is not so small, it is assumed that the influence of the free surface is small and symmetry condition is employed to simulate the free surface effect approximately.

Under bollard condition, the turbulence intensity is zero on the domain boundaries as they are far away from the tunnel thruster. However, to stabilize the computation it was found necessary to impose a small amount of turbulent kinetic energy of $6\times10^{-6}$ $(m/s)^2$ on the velocity inlets. The flow field is initialized by using the full multi-grid method to accelerate convergence.

## 4 NUMERICAL RESULTS AND ANALYSIS

### 4.1 Grid dependence study

Impeller model No.1323 ($A_E/A_O$=0.6, $P_{0.7R}/D$=1.25), which has the largest extended blade area ratio and pitch ratio, and the smallest section thickness-to-chord ratio, has been selected for the study as it is the most challenging in terms of grid generation. Due to the type of grids used around the impeller blades it is impossible to perform a rigorous grid uncertainty analysis. Alternatively, three grid models with different grid densities around the impeller blades and named as GM-A, GM-B, and GM-C respectively have been generated to investigate the influence of grid density on the simulated axial forces and moment. Two parameters are adjusted in the three grid models, i.e. the height of the grid layer adjacent to blade surfaces, and the number of grids along the chord. As shown in Figure 8, the quasi-steady simulations typically converge within 3000 iterations. The axial forces and moment coefficients obtained from the quasi-steady simulations are given in Table 2 together with chordwise grid number, the range of wall-adjacent cell height, and the corresponding average value of y+. The largest relative difference occurs in the torque coefficient, $K_Q$, between GM-A (or GM-B) and GM-C, and is only 0.7%. The differences in $K_T$ and $C_F$ among the three grid models are negligible. As illustrated in Figure 9, the y+ distributions are quite uniform as the wall-adjacent cell height has been adjusted according to the cell's radial location, except for regions near the leading edge as well as blade tip and root. To save computational resources, the wall-adjacent cell height in GM-A is used for all the cases presented hereafter, while the chordwise number of grids is duly adjusted according to the extended area ratio to ensure the same grid density along the chord as in GM-A.

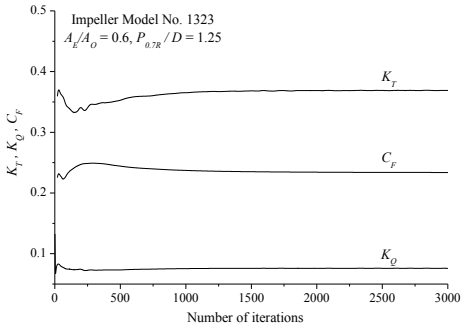


**Figure 8.** Typical convergence histories of $K_T$, $K_Q$, and $C_F$, grid model GM-A, impeller model No.1323, $P_{0.7R}/D$=1.25.

**Table 2.** Influence of wall-adjacent cell height and chordwise grid number on the computed results of axial forces and moment.

| Grid model | Chordwise grid number | Wall-adjacent cell height (mm) | Average $y^+$ | $C_F$ | $K_T$ | $10K_Q$ |
|---|---|---|---|---|---|---|
| GM-A | 210 | 0.01~0.02 | 3.0 | 0.234 | 0.369 | 0.760 |
| GM-B | 300 | 0.01~0.02 | 3.0 | 0.234 | 0.368 | 0.759 |
| GM-C | 210 | 0.005~0.01 | 1.5 | 0.234 | 0.369 | 0.754 |

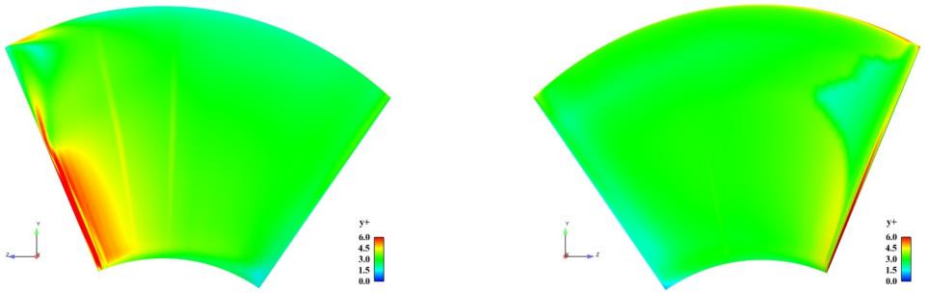

a) suction side b) pressure side

**Figure 9.** Distributions of $y^+$ on blade surfaces, grid model GM-A, impeller model No.1323, $P_{0.7R}/D$=1.25.

## 4.2 Comparison of quasi-steady and unsteady models

It is obvious that the quasi-steady model is more approximate compared. However this model is very economical and can perform quite well when the unsteadiness of flow is not severe. This is the case since there is no gear housing in the tunnel thrusters being computed. The factors which will bring about flow unsteadiness are the interactions of the rotating impeller with the stationary hull and the free surface. These factors are estimated to be quite weak. For verification purposes the quasi-steady and unsteady simulations are carried out for impeller model No.1308, $P_{0.7R}/D$=0.5~1.25.

Taking impeller model No.1308 ($P_{0.7R}/D$=1.25) as an example, the convergence histories of axial forces and moment are shown in Figure 10, where $\overline{K_T}$, $\overline{K_Q}$, and $\overline{C_F}$ denote, respectively, the time-averages of the unsteady $K_T$, $K_Q$, and $C_F$ over each revolution of the impeller blades. Both $\overline{K_T}$ and $\overline{K_Q}$ converge well after 15 revolutions. However, 60~70

revolutions are required for $\overline{C_F}$ to become more or less converged.

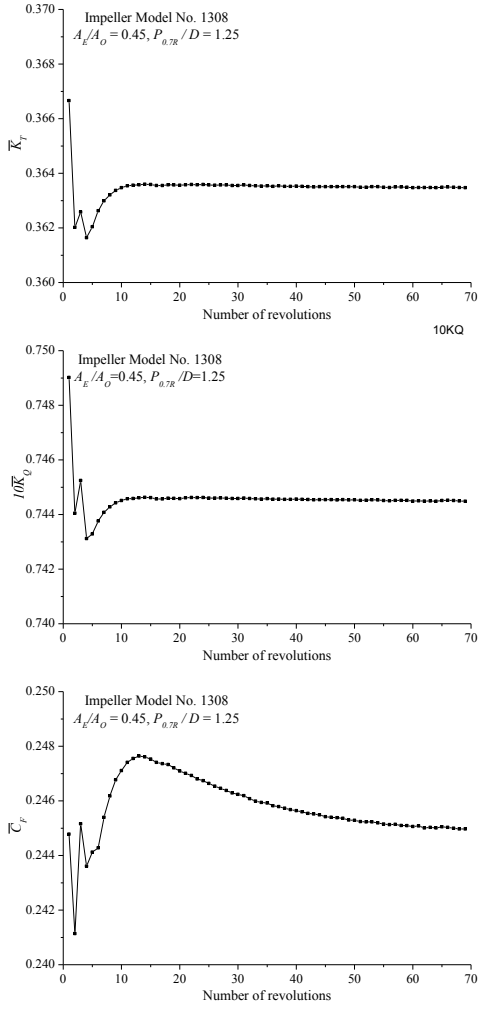


**Figure 10.** Convergence histories of the axial forces and moment averaged for each revolution of the impeller blades, impeller model No. 1308, $P_{0.7R}/D$=1.25.

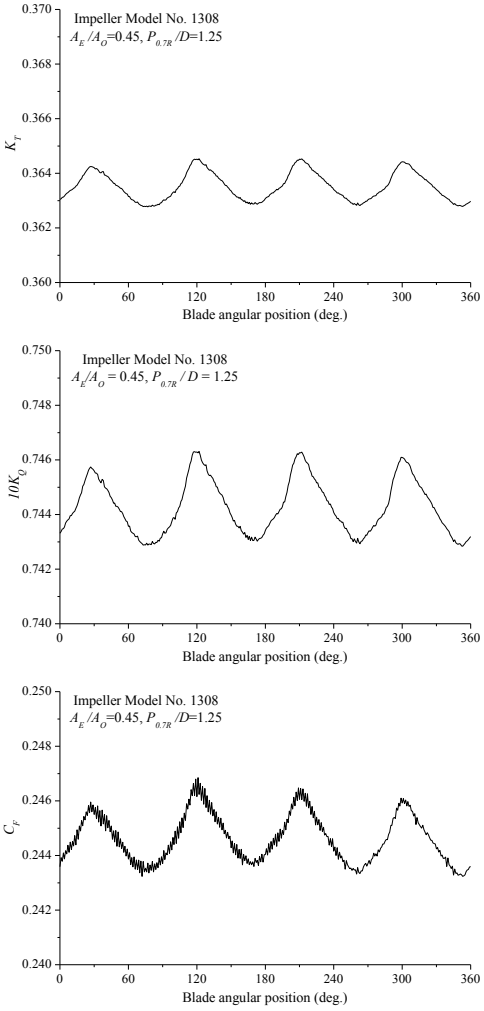


**Figure 11.** Fluctuations of the axial forces and moment with blade angular position in the 70th revolution of the impeller blades, impeller model No. 1308, $P_{0.7R}/D$=1.25.

Figure 11 shows the unsteady axial forces and moment in the 70th revolution of the impeller blades. The unsteady $K_T$, $K_Q$, and $C_F$. all fluctuates in four cycles during one revolution, the fluctuating amplitudes of which, as fractions of the respective time-averages over one revolution, are about $5.5\times10^{-3}$ for $K_T$, $4.0\times10^{-3}$ for $K_Q$, and $10.2\times10^{-3}$ for $C_F$. As can be seen in Figure 15 (b) and Figure 18, the trailing vortex wakes of the four impeller blades induce a quite inhomogeneous four-cycle flow which persists downstream and further induces a nearly four-cycle pressure distribution around the exit of the notional hull, which should be the main reasons for the force fluctuations, especially in $C_F$.

In Table 3 the axial forces and moment coefficients obtained from the quasi-steady and the unsteady simulations are compared with the experimental data from Taniguchi, *et al*.[3] for impeller model No. 1308 over the range of $P_{0.7R}/D$=0.5~1.25. The sliding mesh results are time-averaged over the 70th revolution of impeller blades. The errors are within ±4.5% for

quasi-steady simulations, and within ±8% for unsteady simulations. Looking at the total axial force, $K_T$+ $C_{F.}$, the quasi-steady and unsteady results differ by 0.7%, and both of them differ from the experimental data by less than 1%, except for $P_{0.7R}/D$=1.0.

**Table 3.** Comparison of quasi-steady and unsteady simulation results of axial forces and moment with experimental data, impeller model No.1308, $P_{0.7R}/D$=0.5~1.25.

| | $P_{0.7R}/D$ | Experiment | Quasi-steady Model | Error (%) | Unsteady Model | Error (%) | Quasi-steady / Unsteady |
|---|---|---|---|---|---|---|---|
| $K_T$ | 0.5 | 0.092 | 0.088 | -4.2 | 0.087 | -6.5 | 1.011 |
| | 0.75 | 0.181 | 0.177 | -2.1 | 0.173 | -4.7 | 1.023 |
| | 1.0 | 0.264 | 0.278 | 4.7 | 0.270 | 2.2 | 1.030 |
| | 1.25 | 0.377 | 0.377 | 0.0 | 0.364 | -3.6 | 1.036 |
| $K_Q$ | 0.5 | 0.125 | 0.127 | 1.9 | 0.125 | 0.1 | 1.016 |
| | 0.75 | 0.262 | 0.263 | 0.5 | 0.257 | -1.7 | 1.023 |
| | 1.0 | 0.468 | 0.481 | 2.9 | 0.470 | 0.6 | 1.023 |
| | 1.25 | 0.769 | 0.767 | -0.3 | 0.745 | -3.3 | 1.030 |
| $C_F$ | 0.5 | 0.042 | 0.044 | 4.5 | 0.046 | 8.3 | 0.957 |
| | 0.75 | 0.093 | 0.095 | 2.6 | 0.101 | 8.1 | 0.941 |
| | 1.0 | 0.157 | 0.159 | 1.4 | 0.170 | 7.5 | 0.935 |
| | 1.25 | 0.227 | 0.228 | 0.2 | 0.245 | 7.1 | 0.931 |
| $K_T+C_F$ | 0.5 | 0.134 | 0.132 | -1.5 | 0.133 | -0.7 | 0.992 |
| | 0.75 | 0.274 | 0.272 | -0.7 | 0.274 | 0.0 | 0.993 |
| | 1.0 | 0.421 | 0.437 | 3.8 | 0.440 | 4.5 | 0.993 |
| | 1.25 | 0.604 | 0.605 | 0.2 | 0.609 | 0.8 | 0.993 |

In the rightmost column of Table 3, it is shown that the quasi-steady $K_T$ and $K_Q$ are 1~3% higher than the unsteady ones, while the quasi-steady $C_F$ is 5~7% lower than the unsteady one. In the RANS simulations for ducted propeller and rudder interaction, Sánchez-Caja, *et al*. [11][12] found that, using the quasi-steady model, there was a *numerical blockage effect* that caused an over-prediction of propeller loads due to the interface between the rotating and stationary blocks. Their numerical tests indicate that the interface should be located far from the solid boundaries in order to reduce the numerical blockage effect. In the present case, the interfaces between the rotating and stationary parts are both 1.0$D$ upstream and downstream of blade reference lines (see Figure 4), or more than 0.5$D$ away from blade leading and trailing edges. Such a distance is far larger than that in the propeller-rudder case, and the influence of the numerical blockage effect ought to be quite small. Therefore, it remains to be elucidated why the impeller loads predicted by the quasi-steady model are higher than those by the more accurate unsteady model.

### 4.3 Quasi-steady results for a range of blade areas and pitch settings

Considering the high computational cost of the unsteady model, the quasi-steady model is

employed in further simulations for impeller model Nos. 1322 and 1323, in addition to No. 1308. The comparison of numerical and experimental results is shown in Figure 12. Both results indicate that the influence of blade area is not large, whereas the axial forces and moment all increase nonlinearly with the pitch.

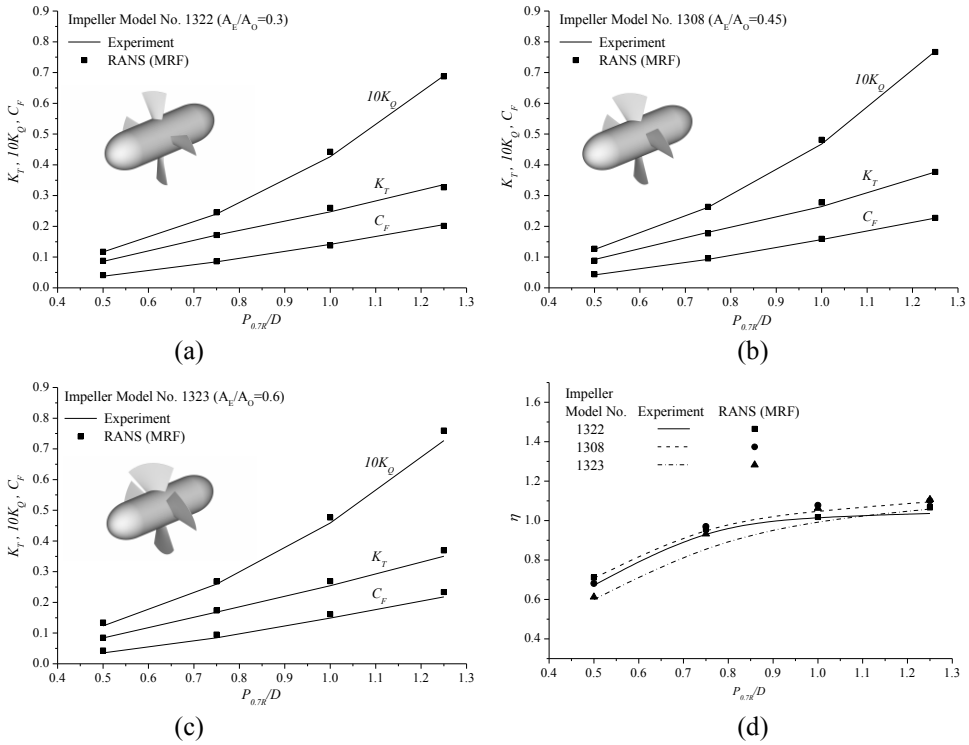


**Figure 12.** Comparison of the simulated hydrodynamic performances and experimental data for impeller Nos. 1322, 1308, and 1323..

As shown in Figure 12 (a), (b), and (c), the RANS-simulated axial forces and moment agree reasonably well with the experimental data in Taniguchi, *et al*.[3]. For the four pitch and three blade area ratios, the errors in predicted $K_T$ and $K_Q$ is within 5%. For impeller model No.1308, the computational error in $C_F$ is negligible. While for impeller model Nos. 1322 and 1323, respectively, the computational results of $C_F$ are slightly lower and higher than the experiment data.

In Figure 12 (d), a comparison of the numerical and experimental static merit coefficients is shown for the three impellers. Both results indicate that the static merit coefficient increases with the pitch ratio and seems to approach to some asymptotic value. Over the range of pitch ratios being considered, it seems that impeller model No. 1308, with $A_E/A_O$=0.45, is the most efficient. In practice the pitch and blade area have to be designed according to the requirements for power (or thrust) and cavitation, respectively.

### 4.4 Contribution to impeller thrust from the hub

Different from the case of open propellers, the hub of the impeller contributes to the thrust. As shown in Table 4, the thrust generated by the hub is about 5~6% of the total thrust of the impeller, and increases with the pitch ratio.

**Table 4.** The contribution from the hub to impeller thrust.

| Impeller Model No. | $A_E/A_O$ | $P_{0.7R}/D$ | 0.5 | 0.75 | 1.0 | 1.25 |
|---|---|---|---|---|---|---|
| 1322 | 0.3 | $\frac{T_{HUB}}{T}\times 100\%$ | 4.7 | 5.6 | 5.9 | 6.2 |
| 1308 | 0.45 | | 4.8 | 5.7 | 6.0 | 6.2 |
| 1323 | 0.6 | | 4.8 | 5.6 | 5.9 | 6.1 |

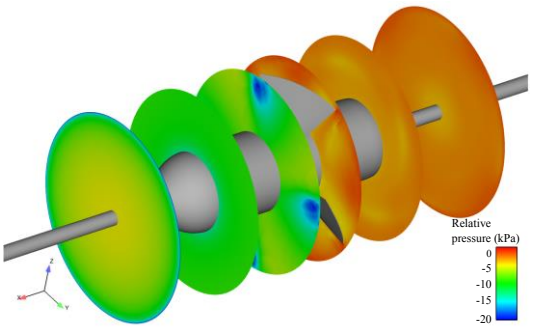


**Figure 13.** Relative pressure distributions along the tunnel, impeller model No. 1308, $P_{0.7R}/D$=1.25.

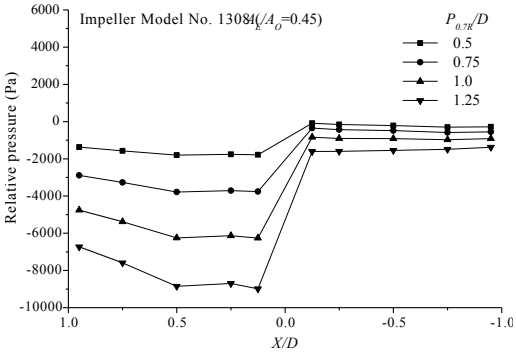


**Figure 14.** Averaged pressure distributions along the tunnel, impeller model No. 1308, $P_{0.7R}/D$=1.25

In Figure 13 the distributions of pressure relative to the ambient pressure are shown at several cross sections inside the tunnel, taking impeller model No. 1308, $P_{0.7R}/D$=1.25 for example. The pressures are averaged over each cross section for the same impeller model at four pitch settings, and the resultant axial distributions of mean pressure inside the tunnel are shown in Figure 14. From the two figures it is easily understood that the rotating impeller blades create a low pressure region upstream, while the pressure downstream keeps very close to the ambient pressure. It is this pressure jump across the impeller blades that results in the hub thrust. The pressure jump increases with blade pitch, see Figure 14, which is consistent with the data shown in Table 4.

### 4.5 The impeller-induced axial force on the hull

To understand how the impeller induces an axial force on the hull, the pressure distributions around the entrance and exit of the tunnel are shown in Figure 15 (a) and (b), respectively. The radial gradient of pressure is very large around the lip of the entrance, but very small around that of the exit.

A quantitative analysis is made by dividing the hull surfaces around the tunnel entrance and exit into a series of concentric donut-shaped patches having a constant width of 0.05$D$, as illustrated in Figure 15 (a). The sum of the axial forces acting on a pair of donut-shaped patches at the entrance and exit sides of the hull is presented as the percentage share of the total axial force acting on the notional hull and plotted in Figure 16. The results indicate that the first three donut-shaped patches contribute about 75% of the impeller-induced axial force. Therefore, it is the steep low pressure region very close to the lip of the entrance that results in the axial force on the hull. This axial force is always in the same direction as the impeller

thrust, and its magnitude is about 50~60% of the impeller thrust, as seen in Table 3 and Figure 12. In this region special attention should be paid to the design of the geometry and structure and, in numerical simulation, to grid size and quality in order to maintain adequate accuracy in predicted axial force.

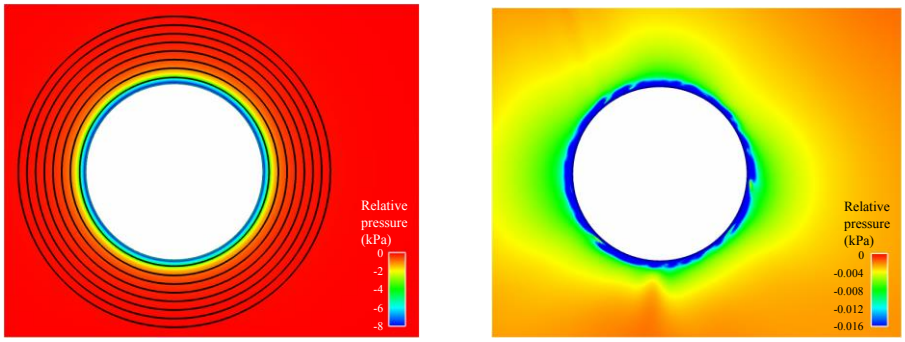


(a) (b)

**Figure 15.** Pressure distributions around (a) the entrance, and (b) the exit of the tunnel, impeller model No. 1308, $P_{0.7R}/D$=0.75.

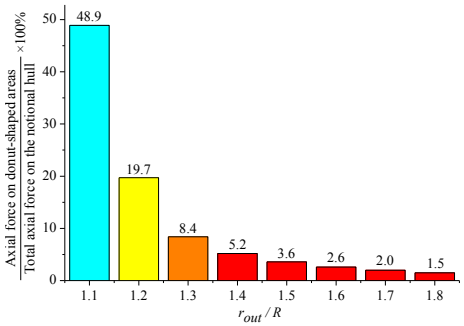


**Figure 16.** Contribution to the axial force on the hull from the donut-shaped areas at different radii, impeller model No. 1308, $P_{0.7R}/D$=0.75.

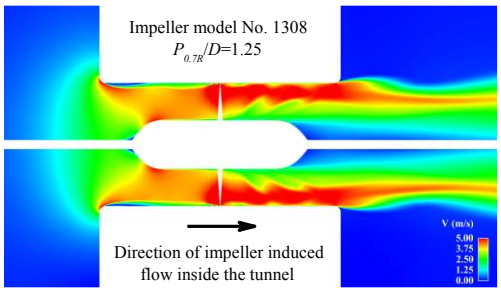


**Figure 17.** Contours of velocity magnitudes in the plane $Z$=0, impeller model No. 1308, $P_{0.7R}/D$=1.25.

## 4.6 Other flow features of interest

In Figure 17 the contours of velocity magnitudes in the plane $Z$=0 are plotted for impeller model No. 1308, $P_{0.7R}/D$=0.75. In Taniguchi, *et al.*[3] the authors believed that the flow separation near the entrance of the tunnel could be avoided with the rounded corner. The present simulation results shown in Figure 17 suggest this is probably not true. Flow separation occurs over quite a distance downstream of the entrance, so the entrance geometry may need to be improved. Besides, a dead-water zone behind the hub is observed in the numerical results which is due to the sudden expansion of the cross-sectional area of flow, and extends far behind the tunnel exit.

To investigate how the impeller-induced flow evolutes, the in-plane velocity vectors together with axial velocity contours are plotted in Figure 18 at several cross-sections for impeller model No.1308, $P_{0.7R}/D$=0.75. Section A and F are located very close to tunnel entrance and exit, respectively. The fluid is sucked into the tunnel in the negative $X$ direction. In section A it is seen that a very strong cross flow occurs close to the lip of tunnel entrance,

while the flow is mainly axial and quite uniform over major area of the section. Then the flow is accelerated axially due to the hub as well as the impeller's suction, as seen in section B. In section C strong in-plane flows are induced at locations close to the leading edges of blade tips, which is related to the strong tip leakage vortex as visualized in Figure 19. In sections D~F, a strong circumferential flow is induced by the rotating impeller blades and weakens as it goes downstream; meanwhile the acceleration of flow along the tunnel mainly takes place in the outer radii.

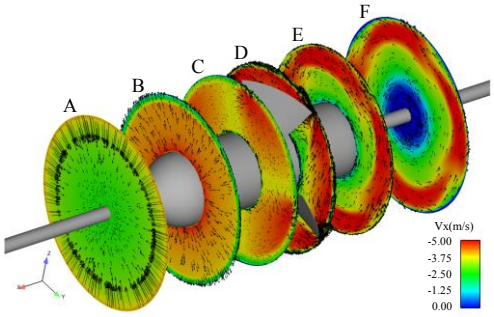


**Figure 18.** In-plane velocities and axial velocity contours at different locations of the tunnel, impeller model No. 1308, $P_{0.7R}/D$=1.25.

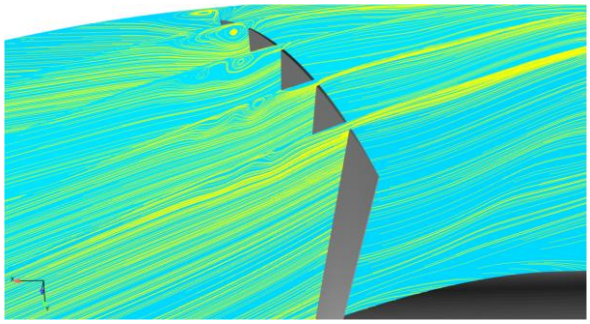

**Figure 19.** The tip leakage vortex visualized with the streamlines derived from the in-plane velocities in the planes perpendicular to the tip section, impeller model No. 1308, $P_{0.7R}/D$=1.25.

## 5 CONCLUDING REMARKS

Two numerical models based on the solution of the RANS equations using the SST $k$-$\omega$ turbulence model have been employed to simulate the hydrodynamic performance and flow of tunnel thrusters. By creating an envelope around each impeller blade, the flow passages between adjacent blades can be discretized with prismatic cells so that the boundary layer flow is resolved down to the viscous sub-layer. The stationary part of computational domain is discretized with block structured hexahedral cells. Based on a grid dependence study suitable values of the chordwise grid size and wall-adjacent grid height are chosen. Numerical simulations are carried out using the quasi-steady model for three controllable pitch impellers with the extended area ratio and pitch ratio ranging from 0.3 to 0.6, and 0.5 to 1.25, respectively. The numerical results of impeller thrust, torque, and the axial force acting on the hull are compared with corresponding experimental results presented in Taniguchi, *et al.*[3], and the agreement between them is reasonably good.

Time-accurate simulations are also performed by using the unsteady sliding mesh model, and the results are compared with those of the quasi-steady model to investigate the influences of the quasi-steady approximation on predicted loads. The impeller thrust and hull axial force predicted by the quasi-steady model are found to be, respectively, larger and smaller than those predicted by the unsteady model. However, the sums of impeller thrust and hull axial force by the two models differ from each other by less than 1%, and both agree well with the experimental data. With the present interface location it should be sufficient to minimize the numerical blockage effect[11][12], and further study is needed to find out the reasons.

Based on the analyses of the axial forces as well as the pressure and velocity distributions

inside the tunnel, the mechanisms behind two peculiar features associated with the tunnel thruster have been made clear. The hub generates a small amount of thrust which increases with blade pitch ratio due to the pressure jump across the impeller blades; and the hull also generates a thrust, which can be as large as 40~60% of the impeller thrust, mainly due to the sharp low pressure peaks acting on a very small donut-shaped area around the lip of the tunnel entrance. Other flow features of interest are also discussed, including flow separation near the tunnel entrance, evolution of the impeller induced flow along the tunnel, and the tip leakage vortex.

The free surface effect is accounted for in the present work by using the flow symmetry condition. In cases when the impeller loading is high enough to cause violent deformation of the free surface, or when there are incoming waves and hull motions, rigorous treatment of the free surface will become necessary. Besides, the impacts of gear housing on cavitation and its induced effects are also important topics. These will be our future work.

## REFERENCES


[1] Carlton, J. S., 2012. *Marine propellers and propulsion*. London: Butterworth-Heinemann, 334-342.

[2] Pehrsson, L. and Mende, R. G., 1961. Design, model testing and application of controllable pitch bow thrusters. *Journal of the American Society for Naval Engineers*, **73**(4): 787-796.

[3] Taniguchi, K., Watanabe, K., and Kasai, H., *et al.*, 1964. Investigation into the fundamental characteristics and operating performances of side thruster, *Report of Shipbuilding Assocaition of Japan*, Tokyo, Japan.

[4] English, J. W., 1964. *Further considerations in the design of lateral thrust units*, NPL Report, National Physical Laboratory, London, United Kingdom.

[5] Beveridge, J. L., 1971. *Design and performance of bow thrusters*, Defense Technical Information Center, America.

[6] Ridley, D. E., 1971. Observations on the effect of vessel speed on bow thruster performance. *Marine Technology Society Journal*, **8**(1): 93-96.

[7] Baniela, S. I., 2009. The performance of a tunnel bow thruster with slow speed ahead: A revisited issue, *Journal of Navigation*, **62**(4): 631-642.

[8] Muller, S. B. and Abdel-Maksoud, M., 2007. *Numerical investigation of transverse thrusters*, IST Report, University of Duisburg-Essen, German.

[9] Stefano, G., Luca, S., and Stefano, B., *et al*., 2009. Comparison of experimental measurements and numerical calculations for a propeller in axial cylinder, *First International Symposium on Marine Propulsors*, Norway.

[10] Yao, Z. Q. and Yan, Z. G., 2012. Hydrodynamic performance analysis and verification of transverse thrusters, *Journal of Ship Mechanics*, **16**(3): 236-245.

[11] Sánchez-Caja, A., Pylkkänen, J. V., and Sipilä, T. P., 2008. Simulation of the incompressible viscous flow around ducted propellers with rudders using a RANSE solver, *27th Symposium on Naval Hydrodynamics*, Seoul, Korea.

[12] Sánchez-Caja, A., Sipilä, T. P., and Pylkkänen, J. V. 2009. Simulation of viscous flow around a ducted propeller with rudder using different RANS-based approaches, *First International Symposium on Marine Propulsors (smp'09)*, Trondheim, Norway.